Physics of Plasmas ARTICLE scitation.org/journal/php

Inviscid damping of an elliptical vortex subject to an external strain flow

Cite as: Phys. Plasmas **29**, 052107 (2022); doi: 10.1063/5.0086227
Submitted: 24 January 2022 · Accepted: 28 April 2022 ·
Published Online: 12 May 2022

P. Wongwaitayakornkul,[1,a)] J. R. Danielson,[1] N. C. Hurst,[2] D. H. E. Dubin,[1] and C. M. Surko[1]

AFFILIATIONS

[1]Physics Department, University of California, San Diego, La Jolla California 92093, USA
[2]Physics Department, University of Wisconsin, Madison, Wisconsin 53706, USA

[a)]**Present address:** Department of Physics, Faculty of Science and Technology, Thammasat University, Pathum Thani 12120, Thailand.
Author to whom correspondence should be addressed: pwongwai@tu.ac.th

ABSTRACT

Inviscid spatial Landau damping is studied experimentally for the case of oscillatory motion of a two-dimensional vortex about its elliptical equilibrium in the presence of an applied strain flow. The experiments are performed using electron plasmas in a Penning–Malmberg trap. They exploit the isomorphism between the two-dimensional Euler equations for an ideal fluid and the drift-Poisson equations for the plasma, where plasma density is the analog of vorticity. Perturbed elliptical vortex states are created using $\mathbf{E} \times \mathbf{B}$ strain flows, which are generated by applying voltages to electrodes surrounding the plasma. Measurements of spatial Landau damping (also called critical-layer damping) are in agreement with previous studies in the absence of an applied strain, where the damping is due to a resonance between the local fluid motion and the vortex oscillations. Interestingly, the damping rate does not change significantly over a wide range of applied strain rates. This can be accurately predicted from the initial vorticity profile, even though the resonant frequency is reduced substantially due to the applied strain. For higher amplitude perturbations, nonlinear trapping oscillations also exhibit behavior similar to the strain-free case. In principle, higher-order effects of the applied strain, such as separatrix crossing of peripheral vorticity and interactions with harmonics of the fundamental resonance, are expected to change the damping rate. However, this occurs only for conditions that are not realized in the experiments described here. Vortex-in-cell simulations are used to investigate the possible roles of these effects.

I. INTRODUCTION

Rotational fluid structures known as vortices are common features of flows in geophysical[1–4] and astrophysical[5–7] fluids and magnetized fusion plasmas,[8,9] and they often have profound consequences for transport properties. In many cases, they are subject to external shear and strain flows, which can cause vortex deformation and destruction.[10–13] An applied strain flow is considered here rather than applied shear due to experimental convenience and the important role of strain flows in vortex dynamics.[10,12,14] Vortices are often subject to external strain flows due to other nearby vortical structures, e.g., in many types of turbulent flows and at the poles of Earth and other planets. Both strain and shear are known to cause elliptical vortex deformations and dynamical oscillations, although the shear has the complication of a sign relative to the vortex rotation.[10] In the presence of strain flows, perturbations on vortices can undergo so-called inviscid damping in which the perturbation resonates with elements of vorticity that are at some distance from it.[15–18] In this paper, the process of inviscid damping of perturbations on two-dimensional (2D) vortices in an ideal, inviscid fluid is studied in experimental and numerical simulations with and without externally imposed strain flows.

The experiments exploit the isomorphism between the 2D Euler equations (1) describing an inviscid incompressible fluid and the Drift–Poisson equations (2) describing the $\mathbf{E} \times \mathbf{B}$ drift of an electron plasma in a strong magnetic field,[15,19]

$$\left(\frac{\partial}{\partial t} - \nabla\psi \times \hat{\mathbf{z}} \cdot \nabla\right)\omega = 0, \quad \nabla^2\psi = \omega, \tag{1}$$

where $\omega = (\nabla \times \mathbf{v}) \cdot \hat{z}$ is the vorticity and ψ is the fluid stream function, which is related to the velocity by $\mathbf{v} = -\nabla\psi \times \hat{z}$, and

$$\left(\frac{\partial}{\partial t} - \frac{1}{B}\nabla\phi \times \hat{\mathbf{z}} \cdot \nabla\right)n = 0, \quad \nabla^2\phi = \frac{en}{\varepsilon_0}, \tag{2}$$

where n is the electron density, ϕ is the electric potential, B is the magnetic field strength, e is the electron charge, and ε_0 is the permittivity of free space. The plasma density is the analog of

vorticity, and the electrical potential is the analog of the fluid stream function.

Previous studies of vortex dynamics in plasmas investigated the free relaxation of a vortex subject to asymmetric perturbations.[15,16] A disturbance on a quasi-flat vortex (i.e., a roughly constant interior vorticity profile with a steeper edge gradient) was found to excite a wave packet or quasi-mode which causes the disturbance amplitude to decrease due to dephasing. This phenomenon is referred to as critical-layer or spatial Landau damping in analogy with the well-known kinetic treatment of plasma wave damping.[17,20] Once the initial decay of the perturbation saturates, an algebraic decay (t^{-k}) is predicted at later times;[21–23] however, recurrence of the perturbation due to vortex-element trapping is commonly observed.[16,24] Others have studied the damping of perturbations in a weak strain field rotating with the vortex[18] and a vortex in a strain field that oscillates slowly with respect to the vortex rotation frequency.[25] In the work presented here, the decay of perturbations on a vortex is examined both with and without an externally imposed, non-rotating strain flow with a magnitude that is varied up to near the stability limit.[14] Surprisingly, it will be seen that the applied strain does not change the measured damping rate.

For an elliptical vortex having a flat-top vorticity profile (a so-called vortex patch) subject to a constant strain flow, the equilibrium, the stability condition,[14] and the exact solution for the dynamics[10] have been studied theoretically. Near the strained equilibrium, an elliptical vortex rotates or nutates about equilibrium with a reduced frequency that approaches zero as the strain is increased. The vortex loses stability through a saddle-node bifurcation at a strain-to-vorticity ratio of approximately 0.15. For a smoother vorticity profile, a multi-patch model was developed to describe the evolution of nested or separated patches under strain.[12,13]

For realistic vorticity profiles with finite edge gradients (e.g., a flat core with a lower vorticity outer halo), the strain modifies the equilibrium orbits of the vortex elements in the halo. As a result, any wave-like disturbance is seen by the vortex element as perturbed and containing higher harmonics. Multiple resonant layers are introduced when the wave frequency is a multiple of the orbital frequency of the vortex element. For monotonically decreasing profiles, the higher-order resonances occur at larger radii. It is shown here that these resonances are pushed toward the separatrix, and they do not contribute significantly to the evolution of the quadrupole moment.

An analogous effect has been described in non-neutral plasma studies, where multiple resonances contribute to bounce-harmonic Landau damping of Trivelpiece–Gould waves.[26,27] In those studies, the equilibrium density and potential were modified by an applied squeeze potential using a cylindrical electrode, thus creating an axial barrier inside the plasma. The axial potential variation in that work is analogous to the azimuthal potential variations here. However, the bounce-resonant velocity space Landau damping is stronger since the resonance criterion is $\omega_b(E) = \omega/n$ with wave frequency ω greater than the bounce frequency $\omega_b(E)$. Bounce harmonics $n > 1$ allow the resonance condition to be satisfied for particle energies within the Maxwellian distribution. The difference in 2D Euler flow is that the $m = 2$ mode frequency is lower than the dynamical frequency for particles in the vortex (i.e., an orbital frequency around the vortex center), rather than higher, and so harmonics $n > 2$ have fewer resonant particles rather than more.

In the work described here, the momentum of the electron is dominated by the magnetic vector potential (i.e., $\propto r^2$), so the action-angle coordinate is a canonical transform from the spatial coordinate.[28,29] This is the basis for the analogy between spatial Landau damping and the usual kinetic Landau damping.

The experiments described here use a specially designed Penning–Malmberg trap (described below) to impose a uniform non-rotating external $\mathbf{E} \times \mathbf{B}$ strain flow on electron plasmas, where the flow is generated by applying voltages to the trap electrodes. The capabilities of this 8-Segment Trap (8ST) have recently been exploited to study several 2D vortex dynamical processes.[30–34] As described in Sec. III, the work presented here exploits the fact that the spatial profile of a vortex, and hence vortex-perturbation damping rates, can be varied by adjusting the plasma fill procedure. This control of the damping rate is a key extension over previous work and enables the comparison between the simple damping at a narrow resonant radius.[16] This has allowed us to identify the regimes of applicability of each and to do the comparison of the damping and associated nonlinear trapping oscillations for strain-free vs strained vortices.

This paper first describes a study of the critical-layer damping of a wavenumber $m = 2$ perturbation on a vortex in the strain-free case and investigates the dependence of the damping on the profile of vorticity outside the vortex core. Then, the damping of these vortex perturbations is studied in the presence of an imposed strain flow. Unexpectedly, it is found that the damping rate remains unchanged in the presence of strain, while the frequency of oscillation of the perturbation is reduced. The unchanged damping rate is explained using an eigenmode analysis of the strained equilibrium. In the phase space of the plasma, the action is invariant when the electric field perturbations are applied adiabatically.[29] Because the physical space and phase space are identical for 2D ideal fluid,[28] the vortex elements at the first resonance undergo the same dynamics, preserving the damping rate. At later times, trapping oscillations are observed until the separatrix of the flow field approaches the critical damping layer. Additional damping due to the evaporation of vorticity elements and higher-order resonances, which are observed in numerical simulations, are discussed.

II. THEORY

Free or isolated vortices tend to be circular, and most theoretical studies have focused on damping toward an axisymmetric equilibrium. However, with the application of the non-rotating external strain field with the stream function

$$\psi_{\text{ext}} = \frac{1}{2}\varepsilon(x^2 - y^2), \tag{3}$$

where the spatial coordinates are scaled to the wall radius r_w and ε is a strength of the applied strain, a different approach is necessary. The azimuthal symmetry is broken and the stable equilibrium becomes elliptical. Figures 1(a) and 1(b) show a linear vorticity map with $\omega_0 = 186$ krad/s for a near equilibrium plasma in two different strain fields. Gray lines show the calculated stream function contour lines for the total flow, green lines show the first resonance layers, and black lines show the separatrices. It is useful to describe a perturbative evolution from this new equilibrium using an action-angle variables, $(r, \theta) \rightarrow (I, \varphi)$, where

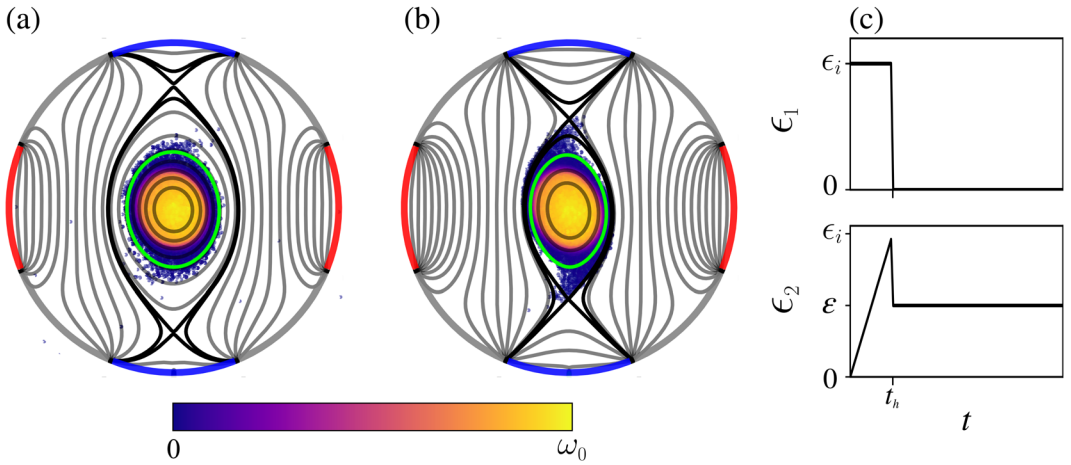

FIG. 1. (a) and (b) Cross section of the electron plasma with applied non-rotating strain boundary $+V$ (red) and $-V$ (blue). The strains applied are (a) $\varepsilon = 0.036$ and (b) $\varepsilon = 0.073$. The first resonant layers are indicated with green lines and the separatrices with black lines. (c) Two time-dependent strain protocols: a square pulse (ϵ_1) and a linear ramp and hold (ϵ_2).

$$I = \oint r^2 d\theta, \tag{4}$$

and

$$\varphi = \Omega_r \int ds/v(s), \tag{5}$$

where I is the canonical action of a vorticity element (i.e., the area enclosed by the orbit), φ is the canonical angle of a vortex element (equivalent to a scaled time in the orbit), s is a distance along the vortex element trajectory, and Ω_r is rotation frequency defined by $\Omega_r = 2\pi/T_r$, where T_r is the orbit period. Note that here, and throughout this paper, all time-related variables (i.e., time, frequency, growth rates, and strain) are normalized by the central vorticity ω_0.

To describe perturbations from the equilibria, we write $\omega = \omega_{\rm eq} + \delta\omega$ and $\psi = \psi_{\rm eq} + \delta\psi$. Then, the linearized Euler equations in canonical action-angle variables are

$$\frac{\partial}{\partial t}\delta\omega + \Omega_r(\varepsilon, I)\frac{\partial}{\partial\varphi}\delta\omega - \frac{\partial}{\partial\varphi}\delta\psi\frac{\partial}{\partial I}\omega_{eq}(I) = 0, \tag{6}$$

$$\nabla^2\delta\psi = \delta\omega, \tag{7}$$

where $\Omega_r(\varepsilon, I) \equiv \partial_I\psi_{eq}$ is the rotation frequency.

As discussed in Sec. III, the two protocols illustrated in Fig. 1(c) are used to apply the strain. A square-wave step is used to decrease the strain from a larger value (ϵ_1) to zero, and an increasing linear ramp and hold (ϵ_2) is used to set the strain at a finite value.

$$\epsilon_1(t) = \epsilon_i\Theta(t_h - t), \tag{8}$$

$$\epsilon_2(t) = \epsilon_i(t/t_h)\Theta(t_h - t) + \varepsilon\Theta(t - t_h), \tag{9}$$

where ϵ_i, and ε are the strains, t_h is the start of the holding time, and Θ is a Heaviside step function. Examples of these functions are shown in Fig. 1(c).

The strain protocol ϵ_1 is used to excite elliptical vortex deformations and then study strain-free damping, whereas ϵ_2 is used to adiabatically prepare a strained vortex state near the elliptical equilibrium in order to study damping in the presence of an applied strain.[34]

For free relaxation ($\varepsilon = 0, I \to r, \varphi \to \theta$), the quasi-mode damping rate of a quasi-flat vortex can be calculated analytically using Eqs. (6) and (7). Briggs, Daugherty, and Levy (BDL)[15] derived the analytic expression, shown in Eq. (10), by substituting Eq. (7) into Eq. (6) and applying an inverse Laplace transform to solve the initial value problem. With the assumption that the initial plasma is quasi-flat with a weak negative-gradient halo, BDL evaluated the dispersion relation by defining a deformed analytically continued Bromwich contour and calculating the principle part of the integral from an imaginary pole.[15] The damping rate ($\gamma_{\rm BDL}$) is

$$\gamma_{\rm BDL} = -\frac{\pi}{4m} r_0\omega'(r_c)\left(\frac{r_0}{r_c}\right)^{2m-3}\left[1 - \left(\frac{r_c}{r_w}\right)^{2m}\right]^2, \tag{10}$$

where m is the azimuthal mode number of the wave, r_0 is the radius of the vortex, $\omega'(r)$ is the radial derivative of the vorticity, and r_c is the critical radius at which the resonance occurs. In this paper, we focus on perturbations with $m = 2$.

The BDL approach depends on the local vorticity at the critical layer. A second approach, that is global in radial coordinate, is the eigenmode theory of Schecter *et al.*[16] These authors generalized the first approach to describe an arbitrary initial profile with a monotonically decreasing density. They decomposed the perturbation in terms of a Fourier series in polar coordinates (r, θ). The result is that each azimuthal mode m decouples. The excitability spectrum is calculated by solving an eigenvalue equation $\mathcal{I}[\xi] = \nu\xi$, where ξ is an eigenvector, ν is an eigenvalue frequency, and $\mathcal{I}$ is a linear operator, derived from Eqs. (6) and (7) and defined as

$$\mathcal{I}[\xi] = 2\Omega_r(r)\xi(r) - \frac{2}{r}\omega'_{eq}(r)\int dr' r' G(r|r')\xi(r'). \tag{11}$$

Here, G is the Green's function for the Laplacian, incorporating the boundary condition $\delta\psi = 0$ at the wall. The excitability is then defined as[16,35]

$$X_k = \frac{\int dr r^3 \xi}{\int dr r^2 \xi^2 / |\omega'_{eq}(r)|}. \tag{12}$$

Experimental data, $\omega(r)$, comes in through $\omega'(r)$ and $\Omega_r(r)$, which is an unperturbed orbit rotation frequency and is an integral of $\omega(r)$, i.e., $\Omega_r(r) = (1/r^2)\int_0^r dr' r' \omega(r')$. The damping rate can be calculated from the width of the excitability spectrum, assuming that the spectrum is Lorentzian, i.e., $X_k \sim 1/[(\nu_k - \nu_d)^2 + \gamma^2]$, where X_k is the amplitude of an exciting mode, ν_k is mode frequency, ν_d is the center of the spectrum, and γ is the spectrum width.

In the presence of an external strain, the damping rate is expected to depend upon $\Omega_r(\varepsilon, I), \partial_\varphi \delta\psi$, and $\partial_I \omega_{eq}(I)$. The exact analytical expression is not known. However, for an $m = 2$ perturbation, it can be measured experimentally by calculating a quadrupole moment Q from

$$Q(t) = \int d^2 r r^2 e^{-2i\theta} \delta\omega(t), \tag{13}$$

$$Im(Q(t)) = Q_{eq} + Q_0 e^{-\gamma t} \sin(\nu_d t + \theta_0), \tag{14}$$

where Q_{eq} is the quadrupole moment at the equilibrium and ν_d is an oscillation frequency of the quadrupole moment. Equation (14) describes the behavior of the imaginary part of Q in a strain strain field. For a vortex patch near the strained equilibrium, Moore and Saffman (MS)[14] calculated the frequency $\tilde{\nu}_d$

$$\tilde{\nu}_d^2 = \frac{1}{4}\left[\left(\frac{2m\lambda}{\lambda^2+1} - 1\right)^2 - \left(\frac{\lambda - 1}{\lambda + 1}\right)^{2m}\right], \tag{15}$$

$$\tilde{\nu}_d \approx (1/2)\left[1 - 16\varepsilon^2 - 100\varepsilon^4 + \mathcal{O}(\varepsilon^6)\right], \tag{16}$$

where λ in Eq. (15) is the aspect ratio of the elliptical vortex patch at the equilibrium. Equation (16) shows the approximate dependence of $\tilde{\nu}_d$ on the strain for $m = 2$. For a smooth vortex, $\nu_d < \tilde{\nu}_d$.

A strained equilibrium can be achieved by adiabatically increasing the strain flow to a final strain value.[34] For a quasi-flat initial profile, a simple external strain flow transforms a circular vortex core into an ellipse that rotates or nutates about the equilibrium. In equilibrium, the contour of the vorticity and the stream function is coincident [i.e., $\omega = \omega(\psi)$].

With applied strain, the equilibrium spatial distribution of the vorticity (or plasma density) differs than that without strain. However, in action-angle coordinates, $\omega(I)$, and consequently $\partial_I \omega(I)$, are the same in both cases due to adiabaticity. In contrast, the vortex element orbit is modified by the strain and is approximately elliptical for an $m = 2$ strain flow sufficiently far from the separatrix. The orbit frequency (Ω_r) is modified by the strain in the same way as the vortex element on the boundary of the vortex,[12] i.e.,

$$\Omega_r(\varepsilon, I) = I_0/(2I) - 8\varepsilon^2 + \mathcal{O}(\varepsilon^4). \tag{17}$$

For a vortex patch, the orbit frequency at the vortex boundary matches the nutation frequency of the ellipse, i.e., $\Omega_r(\varepsilon, I_0) = \tilde{\nu}_d(\varepsilon)$, where $\tilde{\nu}_d(\varepsilon)$ is given by Eq. (16). Note that this condition is different than the resonance condition, which involves the angular symmetry number n described later in Eq. (19).

Until now, the focus has been on the dominant perturbation of the core. However, if an $m = 2$ distortion is introduced on the surface of the vortex, vortex elements in the halo not only experience an $n = 2$ perturbation to their potential along the orbit, but also $n = 4, 6, 8, \ldots$, perturbations due to the added strain, where n is the potential-perturbation mode number. Here, n is restricted to even integers due to the $e^{2i\theta}$ symmetry of the strain.

Non-strained vortices do not experience these higher-order harmonics. Even though the vortex element rotation frequency decreases away from the vortex, there are no $n > 2$ perturbations for streamlines that match multiples of the nutation frequency.

The perturbation of the stream function can be written as the expansion

$$\delta\psi^{(m,n)}(I, \varphi) = \sum_n \sum_m \mathcal{A}_{(m,n)}(I) e^{in\varphi}, \tag{18}$$

in terms of the expansion coefficients $\mathcal{A}_{(m,n)}(I)$.

The $n = 2$ perturbation dominates for I near the vortex core, while the $n > 2$ perturbations become important at larger values of I closer to the separatrix (i.e., where the fluid moves more slowly). The resonance condition is

$$\nu_{d,m}(\varepsilon) = n\Omega_r(\varepsilon, I_{c,n}), \tag{19}$$

where $\nu_{d,m}(\varepsilon)$ is the frequency of the quasi-mode, m and n are even integers, and $I_{c,n}$ is the critical action of a nth-order resonance. For monotonically decreasing profiles, this implies that the higher-order resonances occur at larger radii. Thus they are pushed toward the separatrix, and they do not contribute significantly to the evolution of the quadrupole moment.

If the resonances overlap, then the motion of vortex elements can become chaotic. This phenomenon is known as the stochastic instability or Chirikov criterion.[36] This is a general mechanics result with applications in plasma physics[37] as well as planetary orbits.[38] Its effect on the vortex damping is presently unclear and beyond the scope of the work discussed here.

For a quasi-flat vortex with a small halo close to the vortex core, the major contribution of the wave–vorticity interaction comes from the lowest-order resonant layer, $(n = 2)$. In this case, $\mathcal{A}_{(2,2)}(I) = 1/I$, and it shares the same dependence on I as $\Omega_r(\varepsilon, I)$. At the first resonant layer, this can be thought of as having an action-angle coordinate that is a conformal mapping of the polar coordinate from the original free-damping problem $(r, \theta) \to (I, \varphi)$. The orthogonality is preserved from the conformal map, and the distribution is preserved due to adiabaticity.

The spatial coordinates outside of the strained elliptical core can be conformally mapped to a complex stream function.[12] The real and imaginary components coincide with (I, φ) near the vortex core. Equation (20) describes the mapping of this function onto the complex stream function coordinates, where ω_0 is a central vorticity, A is the area of the vortex core, $w = \cosh^{-1}(-iz/c)$, c is the focal length of an elliptical core, and $z = x + iy$.

$$\Psi = \frac{\omega_0 A}{2\pi}\left(w + \frac{1}{2}e^{-2w}\right) + \frac{1}{2}\varepsilon z^2. \tag{20}$$

However, this is only true due to the fact that the first resonance is dominated by the $n = 2$ perturbation. The free case cannot be mapped exactly into the strain case, because they are topologically distinct. The mapping works only in an approximate sense, far enough from the separatrix that the streamlines are quasi-elliptical. This mapping,

although approximate, will be used in Sec. V D to investigate possible higher-order resonances in the flow.

In addition to the linear dynamics, non-linear effects such as trapping oscillation are also expected. The vortex forms satellite islands in the rotating frame where vorticity is periodically trapped. For free relaxation, the trapping frequency is[16]

$$\omega_b^2 = \frac{m^2}{r_c}|2\delta\psi(r_c)\Omega_r'(r_c)|. \tag{21}$$

In Secs. III–VI, this formalism and the associated formulas developed here will be used to describe the damping rate of $m = 2$ perturbations on a vortex both during free relaxation and in an applied external strain flow. The quadrupole moment will be used to monitor the perturbation amplitude, and it will be compared to the predictions of both BDL and the Lorentzian width of the excitability spectrum obtained from the experimental vorticity profiles. Trapping oscillations are observed, and they are used to verify the restricted regime of linear damping. Furthermore, numerical simulations will be used to study $n = 2$ and $n > 2$ resonances in the halo in order to identify the circumstances where they may affect the damping rate.

III. DESCRIPTION OF THE EXPERIMENT

The experiment is performed in the 8ST,[30–34] which has the electrode geometry shown in Fig. 2(a). The cylindrical electrodes surrounding the plasma have a length $L = 0.26$ m and radius $r_w = 13$ mm. The applied magnetic field is $B \sim 4.8$ T, and the background pressure is 10^{-9} Torr. Eight azimuthal electrode segments extend over the entire plasma. Voltages $V(r_w, \theta)$, on these segments, are used to apply the time-dependent strain flows illustrated in Fig. 1(c), where the total flow field is shown superimposed on the measured vorticity map. Clockwise from the top, the voltages are $(-V, 0, +V, 0, -V, 0, +V, 0)$. The magnitude of the resulting applied $\mathbf{E} \times \mathbf{B}$ quadrupole strain flow is $\varepsilon \approx 1.8V/Br_w^2$ (SI units). The plasma is diagnosed by accelerating the electrons onto a phosphor screen biased to +5 kV and recording the image with a CCD camera. The corresponding spatial resolution of the vorticity measurement is 65 μm/pixel.

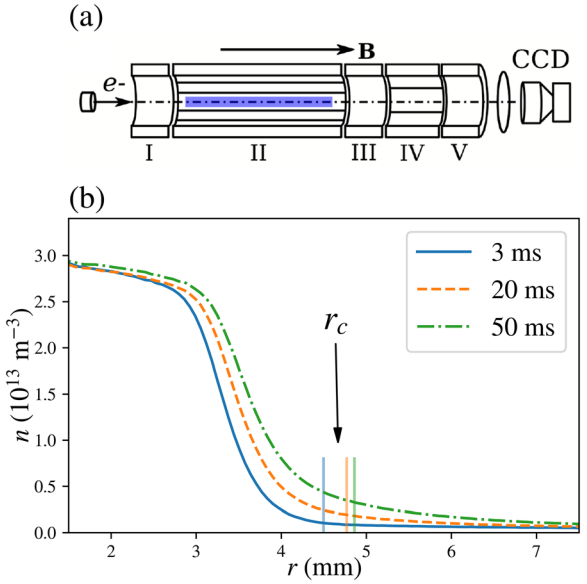

FIG. 2. Schematic diagram of the experimental setup. (a) columnar plasma inside the cylindrical Penning–Malmberg trap. Various sections of the trap are indicated: (I, III, and V) for axial confinement, (II) 8ST electrodes for the fluid experiment, and (IV) four-sector for RW. The electron gun and CCD are also shown. (b) The initial plasma profile for different fill times: 3, 20, and 50 ms, with $n(r = 0) = 3.2 \times 10^{13}$ m^{-3} and $r_w = 13$ mm. The resonance radius (r_c) for each profile is indicated.

The electron plasma has a temperature of $T \sim 0.1$ eV,[31] lengths of $L_p = 0.24$ m, number of particles of $N = 1.2 \times 10^8$, and density of $n = 3.0 \times 10^{13}$ m^{-3}. The cyclotron frequency is $f_g = 134$ GHz, bounce frequency $f_b = 300$ kHz, $\mathbf{E} \times \mathbf{B}$ frequency $f_v = 20$ kHz, and the collision frequency is $f_c \sim 3$ kHz. These parameters satisfy the assumptions of the plasma-fluid analogy.[19] All of the experimental data presented here are averages of three fill and dump cycles.

The time-dependent strains used here were defined in Eqs. (8) and (9) with example waveforms shown in Fig. 1(c). The ϵ_2 protocol features a small discontinuity at the end of the adiabatic ramp, which gives rise to a perturbative oscillation about the equilibrium. The damping happens with a constant applied strain and the time dependent strains of ϵ_2 are different ways to achieve the initial condition. The values ϵ_i, ε, and t_h are chosen to keep the initial amplitudes of the perturbation similar across the range of the holding strains ε. Specifically, referring to Fig. 1(c), for $\varepsilon < 0.040$, $\epsilon_i = 0.045$ and $t_h = 2.9$; and for $\varepsilon > 0.040$, $\epsilon_i = \varepsilon \in [0.045, 0.109]$ and $t_h \in [2.9, 8.7]$.

The initial symmetric radial density profile of the plasma (i.e., the vorticity profile) consists of a quasi-flat core ($r_{\text{core}} = 3.5$ mm) and a small amplitude halo ($\omega_{\text{halo}}/\omega_0 < 0.1$) [cf. Fig. 2(b)]. This is accomplished using the rotating wall (RW) technique[39] to tailor the core plasma, while the vorticity halo is varied using radial transport controlled by changing the time of the electron fill process, as illustrated in Fig. 2(b).

The three vorticity profiles used in this work are shown in Fig. 2(b) where the slope at the resonant radius (labeled r_c) increases as the fill time is increased. Longer fill times result in more diffuse profiles with larger gradients at the critical layer and thus stronger damping. The central vorticity is only slightly modified, so the scaled time and strain are approximately the same for the three profiles.

Using the profiles shown in Fig. 2(b), the slope at r_c can be found by fitting to a linear curve, and this can be used in Eq. (10) to obtain the BDL predicted damping rate for each initial condition. Likewise, as described above, the excitability spectrum can be found by integrating the profiles and then fitting a Lorentzian to obtain the predicted γ_l. The measured damping is found by imaging the vortex at variable times after the application of the strains shown in Fig. 1(c). Then, the amplitude of the $m = 2$ perturbation at each time is obtained by calculating the quadrupole moment using Eq. (13). To minimize spurious effects due to the noise floor of the images, the profiles shown in Fig. 1(c) are clipped at the 8% level before applying the fit.

IV. FREE DAMPING ($\varepsilon = 0$)

Vortex relaxation from an $m = 2$ perturbation on a symmetric vortex is investigated using electron plasma in the 8ST device.[30–34] Although this situation has been studied a number of times, a central feature of the work presented here is the ability to tailor the initial radial profile to be quasi-flat while also controlling the halo using the plasma fill time, as shown in Fig. 2(b). This procedure results in changing the damping rate while nominally leaving the vortex core fixed.

The results are shown in Fig. 3(a), where the time dependence of the quadrupole moment is measured for three different initial conditions. Each data set is fit to an exponentially decaying quadrupole moment given by $Q(t) = Q_0 e^{-\gamma_o t}$, with decay constant γ_o. The normalized quadrupole moment is $\bar{Q} \equiv Q(t)/Q_0$.

The decay rate was obtained for a wide range of fill times, and the resulting measured rates are shown in Fig. 3(b). The measurements are compared to the two theoretical descriptions described in Sec. II.[15,16] Both approaches predict that the initial amplitude of the quadrupole moment decays exponentially. When the initial pulse is small enough ($\lambda_0 < 1.5$), the decay rate is observed to be independent of the initial amplitude ($\delta\gamma/\gamma_0 < 2\%$). The calculated BDL prediction (γ_{BDL}) is obtained from the slope, and the Lorentzian width (γ_l) from the excitability spectrum, for each fill time.

For weaker damping rates (fill times < 40 ms), the measured damping rate increases with fill time and agrees well with both predictions. However, for longer fill times, the damping rate no longer increases, and the measured rates diverge from the BDL predictions. In these cases, the profile becomes smoother, and the approximation of a simple perturbation is no longer valid. This can be seen by looking at the excitability spectrum for longer fill times, as shown in Fig. 3(c). For longer fill times, the perturbation is extended over a significant portion of the profile, and the spectrum can no longer be described by a simple Lorentzian nor by a narrow resonant layer. It should be noted, however, that although the BDL approximation breaks down, the width of the excitability (γ_l) is still observed to be close to the measured damping rate.

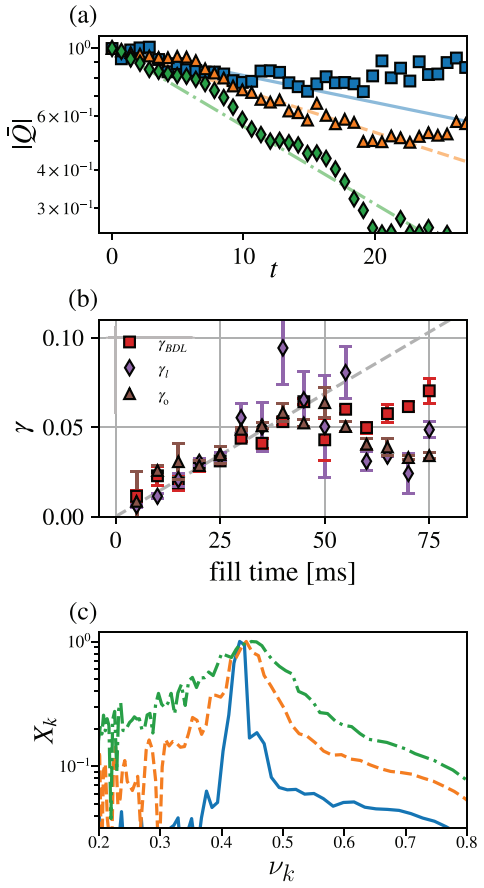

FIG. 3. (a) Experimental data for the time dependence of the quadrupole moment for fill times of 3 (blue, □, solid), 20 (orange, △, dash), and 50 (green, ◇, dashdot) ms; (b) comparison between γ_{BDL}, γ_l, and γ_o for fill times 3–75 ms. Dash line represents a slope of 1.4 s^{-1}, and (c) the excitability spectrum calculated using Eq. (12) for the three fill times in (a).

Finally, looking at the late time evolution for the weaker damping cases in Fig. 2(c), it can be seen that the decay slows down and reverses. This reversal is due to the trapping oscillations. The frequency of the trapping oscillations is observed to be proportional to the square root of the amplitude as is predicted theoretically.[16]

The results in this section are consistent with prior work, and they (empirically) identify the range of parameters in which these theories are valid. The more complicated and novel case of damping in an applied strain field is investigated in Sec. V.

V. STRAINED DAMPING ($\varepsilon > 0$)

In this section, the damping of a quadrupole perturbation in the presence of an applied strain is investigated. Experimental measurements of the damping and trapping oscillations are presented. They show that, to the lowest order, the damping and trapping are independent of the applied strain. Simulations are described to probe the limits of this independence. They are also used to investigate the evaporation of vorticity across the separatrix and the influence of higher-order resonances on the flow field.

A. Experimental results for quadrupole perturbations

A quadrupole perturbation is created on an initially axisymmetric vortex using the protocol ϵ_2 shown in Fig. 1(c). In this case, the vortex is adiabatically strained to an initial amplitude of ellipticity, and then a second (smaller) static strain is applied. The distorted vortex oscillates about the equilibrium defined by the static strain and damps toward that equilibrium. The focus here is to investigate the manner in which the damping rate is changed due to the amplitude of the static strain.

The time dependence of the amplitude of the quadrupole perturbation in the direction of the strained equilibrium [$Im(Q)$] is shown in Fig. 4 for various values of the applied (static) strain ranging from $\epsilon_2 = 0$ to 0.11. The initial plasma was prepared with a fill time of 30 ms, which was shown in Sec. III to give results that, in the free case, agree well with the theory for the unstrained case. The top curve shows the free case for $\epsilon_2 = 0$, and the bottom curve corresponds to the highest strain studied, $\epsilon_2 = 0.11$. For comparison, the maximum stable strain for a flat vortex is $\epsilon = 0.15$.[14] However, this maximum is reduced when either the strain is applied dynamically or the profile is smooth,[30] as is the case here. Thus, the maximum strain case studied here is close to the stability limit.

The time dependence of the quadrupole moment data shown in Fig. 4 can be fit to a damped oscillator as described by Eq. (14). Each fit provides a measure of the damping rate γ and oscillation frequency ν_d. The measured fit parameters are shown vs the applied strain in Figs. 5(a) and 5(b). For these data, the measured unstrained quasi-mode frequency is $\nu_d = 0.465$ and $\gamma = 0.032 \pm 0.005$. Note that the γ value here is slightly different than that in Fig. 3(b) for a fill time of 30 ms because of differences in other experimental parameters.

As described in Sec. II, the unstrained damping rate is calculated using the BDL expression and the eigenvalue method of Schecter

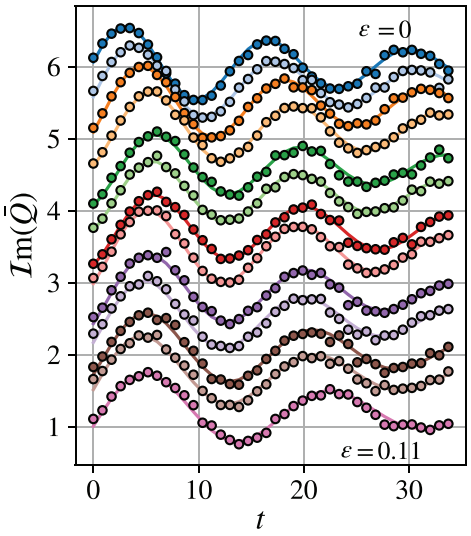

FIG. 4. Evolution of the quadrupole moment normalized by its initial amplitude and shifted vertically for visibility for strain values $\varepsilon = 0 - 0.11$. The top curve is the free case ($\varepsilon = 0$), and the bottom curve is the highest strain value, $\varepsilon = 0.11$. The solid lines are fits the data using Eq. (14).

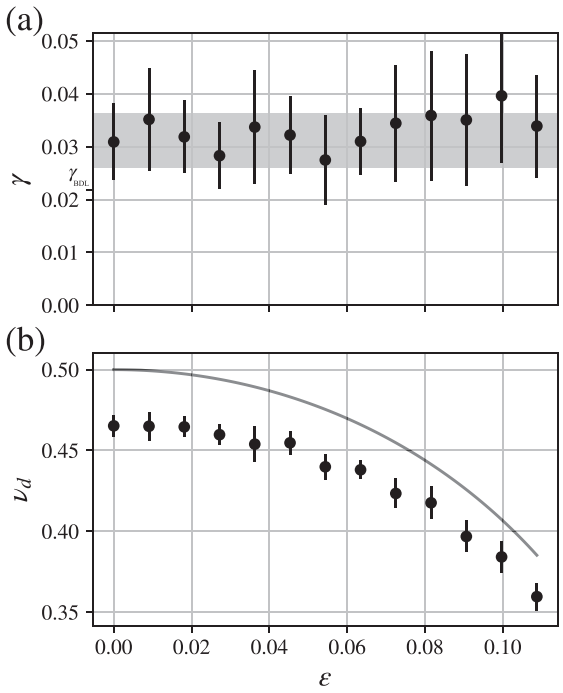

FIG. 5. (a) The fitted decay rate of the quadruple moment; and (b) the fitted mode frequency. The shaded region in (a) indicates the width of the excitability spectrum of the initial condition, and the gray line in (b) is the discrete frequency of an ideal flat vortex $\tilde{\nu}_d$ from Eq. (16).

et al.[16] The excitability spectrum is then calculated, similar to the ones shown in Fig. 3(c). As discussed above, because the spectrum is not well represented by a Lorentzian, there is a larger uncertainty in the value of γ_b, and this is shown as the shaded gray rectangle in the figure.

The measured oscillation frequency is shown in 5(b), and it is compared to the predicted frequency from Eq. (16) which is shown as the solid line. As expected, the rotation frequency of the strained vortex is smaller than that of an unstrained vortex. The theory curve does not match exactly because it was derived assuming an ideal flat vortex, whereas the smoothness of the experimental profile slightly reduces the rotation frequency.

To summarize the results for the strained case, the observations show that, while the frequency of the mode decreases with strain as expected, the damping rate is independent of the value of the strain. In action-angle coordinates, the vortex elements at the first resonance experience the same dynamics from the wave regardless of the strength of the strain [Eqs. (6) and (7)]. The lack of variation with strain is also thought to be due to the absence of a vorticity gradient at higher-order resonances, as well as the lack of vorticity separatrix crossing due to intentionally small vortex perturbations. The role of these effects are discussed further in Secs. V B-D.

B. Trapping oscillations

Trapping oscillations, which are a well known nonlinear effect associated with spatial Landau damping, are commonly observed in experiments.[16,24] They involve the transfer of vorticity into and out of stream function islands in the frame rotating at the vortex oscillation frequency ν_d. The frequency of these oscillations is proportional to the square root of the wave amplitude.[24] The frequency is estimated in Briggs *et al.*,[15] and the result is given in Eq. (21). These oscillations were observed earlier, even for the weakest damping in the strain-free case. Here, we investigate the late time behavior of a mildly strained vortex.

Figure 6(a) shows the long-time evolution (∼50 rotations) of both components of the quadrupole moment ($Im(Q)$ and $Re(Q)$) for a strained vortex at $\varepsilon = 0.025$. Both curves are normalized to the initial quadrupole moment. Since $Im(Q)$ is the component aligned with the strain axis, it oscillates about the equilibrium Q_{eq}, whereas $Re(Q)$ oscillates about zero.

There are not enough data to do a fit to Eq. (14), as was done in the Sec. V A. However, the equilibrium quadrupole moment can be subtracted to obtain the magnitude of the relative normalized quadrupole moment, and these results are shown in Fig. 6(b). The dashed line at early times represents the initial decay rate predicted by the width of the excitability spectrum. At later times, $Q(t)$ oscillates with a period of $t \sim 160$, in agreement with Eq. (21). This and the subsequent recurrences are due to trapping oscillations. Even though trapping is observed, the data are in the regime $\gamma > \nu_d$, which is required for an initial exponential damping to take place.[16]

Although the measurements are limited to fairly small strain rates, the results show that the trapping oscillations, as was true for the linear damping rate, are in the lowest order also independent of the magnitude of the strain.

C. Evaporation

As the separatrix moves closer to the vortex core, the trapping oscillation amplitude can excite trapped elements of vorticity across

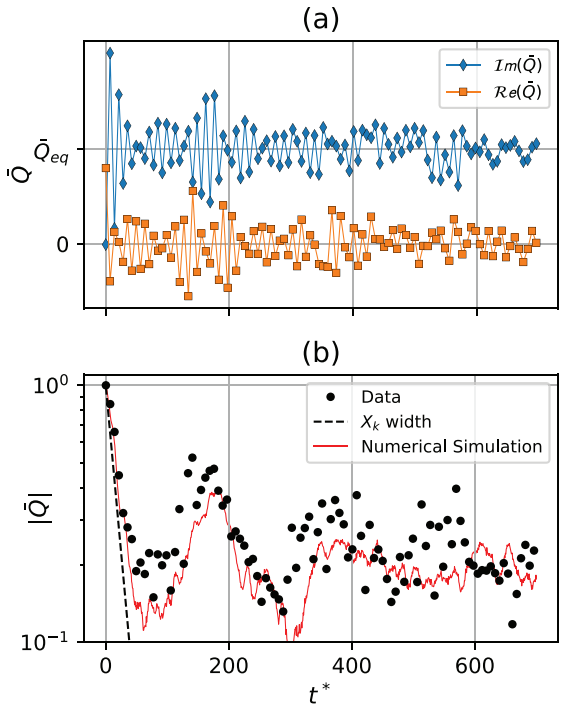

FIG. 6. (a) The two components of the quadrupole moment oscillating over ∼50 rotations for $\varepsilon = 0.025$; and (b) the relative quadrupole moment from the equilibrium compared with numerical simulation data at the same strain rate. The solid line in (a) connects the data points as a guide for the eye.

the separatrix. The lost vorticity carries angular momentum and thus provides an additional (evaporative) damping mechanism. Numerical simulations were used to study this effect. They solve the 2D Euler equations (1) using a particle-in-cell algorithm with Runge–Kutta fourth order time-advance method.[32,40] The simulations are executed on a 600×600 grid with 10^6 particles, and a time step $\Delta t = 0.4$. As in the experiments, the simulations monitor the quadrupole moment for different evolution times. The particles that cross the separatrix are identified, and the number that flows to the wall (N_w) are recorded.

Figure 7 shows the results from a series of numerical simulations of the time dependence for an initially flat-top vortex in the range of larger strains, $\varepsilon = 0.06$–0.11. At these values of strain, the proximity of resonant layer(s) to the separatrix results in elements of vorticity crossing the separatrix (i.e., carrying energy with them), rather than becoming trapped in an island. The time-dependent strain protocol ϵ_2 from Sec. II was used to adjust the value of the strain. Here, $\epsilon_i = \varepsilon$ and $t_h = 3$, 4, 5, 6, 8, and 10, with larger t_h corresponding to larger ε. Figure 7(a) shows the number of particles hitting the wall N_w, which proceeds in an approximately stepwise manner. The particles are preferentially lost at one phase in the Kida orbit where the vortex is stretched nearer to the X-point, causing the stepwise nature of particles hitting the wall. This results in evaporative damping, while the amplitude of the nonlinear trapping oscillations is reduced. This particle loss is similar to that observed in Hurst *et al.*[32] The total number of particles lost is always <4%. The fraction of halo particles is $N_h/N_t = 0.21$. The exchange of particles between the core and halo is small on the time scales studied here.

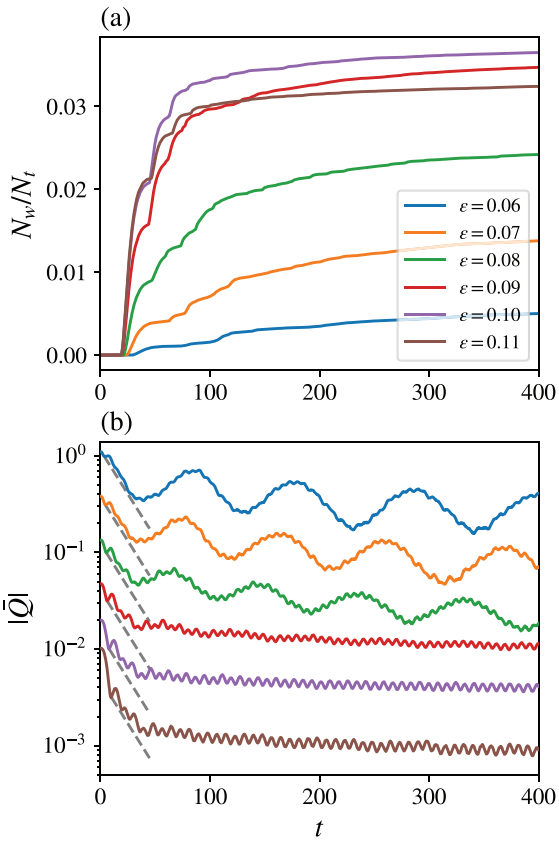

FIG. 7. Simulation of the time evolution of an initially flat-top vortex in the region of strains $\varepsilon = 0.06$–0.11 in which vortex elements (fluid particles) cross the separatrix. (a) the number of particles hitting the wall N_w is normalized by the total number of particles N_t. (b) Time dependence of the quadrupole moment normalized by $Q(t_h)$ with the plots shifted vertically for visibility. The initial decay corresponds to that of the unstrained case [BDL Eq. (9), dash lines]. See text for details.

Figure 7(b) shows the time dependence of the quadrupole moment as a function of time. The initial decay is exponential with a rate that matches the free case. The high frequency oscillation of $|\bar{Q}|$ is the result of nutation of the vortex. For strains larger than $\varepsilon = 0.08$, the quadrupole moment does not produce recurrences, but declines gradually. The presence of strain does not alter the damping and trapping dynamics of the vortex at lower values of strain. However, for $\varepsilon > 0.08$, evaporation leads to the disappearance of the trapping oscillations. This effect is caused by having a separatrix closer to the vortex than the first resonant layer. Therefore, the vortex-elements at the first resonance are no longer bound to a close orbit and escape to the wall (evaporate). A trapping oscillation, which involves these vortex-elements, can no longer exist.

D. Higher-order resonances

Although the experimental conditions were such that the damping was unaffected by higher-order critical layers (i.e., harmonics of the fundamental which appear to be due to the applied strain), numerical simulations have been conducted which are able to study this

effect. The strain was set at $\varepsilon = 0.03$, chosen specifically to visualize the cat's eyes (i.e., the island structures or regions of phase space corresponding to particle trapping with a pattern reminiscent of a cat's eye). The initial state is prepared by distributing point vortices of equal strength using the Monte Carlo technique. The simulation data are taken from time $t = 168$. The initial condition is a flat vortex patch with a small, linearly decreasing halo. Specifically, $\delta r/r_w = 0.25$ and $\omega'(r) = 0.4\omega_0/r_w$, where δr is the radius difference between the halo and the core. For monotonically decreasing radial profiles, the higher-order resonances occur at larger radii. Thus, while the halo slope is chosen to be similar to Fig. 2(b), the halo extends further in radius in order to include the locations of higher-order resonances.

An applied strain introduces higher-order resonances ($n > 2$) that occur when the action of the particles meets the condition specified in Eq. (19) for n an even integer. For a given strain ε, there is a critical action $I_{c,n}$, such that particles resonate with the perturbation mode n, generated by wave mode m. Because Ω_r is strictly decreasing with the value of the action, higher-order resonances occur at larger values of the action, i.e., $I_{c,2} < I_{c,4} < I_{c,6} <, \ldots,$.

To see this effect in the simulations for the $n = 4$ resonance, the halo surrounding the vortex patch is extended to cover the location for $n = 4$ specified by Eq. (19). The $n = 2$ and $n = 4$ resonances correspond to two and four cat's eyes, respectively. The islands in the particle phase space corresponding to these resonances are investigated in Fig. 8. Figure 8(a) shows a snapshot of halo vortex elements colored by their initial radial positions in spatial coordinates (x, y). Figure 8(b) shows a conversion from the spatial coordinates in Fig. 8(a) into the action-angle coordinates described in Sec. II, i.e., $(x, y) \rightarrow (I, \varphi)$. The data are first conformally mapped into a complex stream function, using Eq. (20), and then mapped into the action-angle coordinates. The mapping between the complex stream function and the action-angle coordinate is found from a numerical analysis of the halo in equilibrium. The cat's eyes features of the $n = 2$ and $n = 4$ resonances are shown in Fig. 8(b).

To analyze these features quantitatively, the total number of vortex elements in a range of action, $\mathcal{N} \equiv \int dI\omega(I, \varphi)$, is plotted in Fig. 8(c) in two regions: $I/I_0 \in [1.9, 2.1]$ (blue) and $I/I_0 \in [3.9, 4.3]$ (orange). A peak in φ represents a dense region of vortex elements. The number of peaks indicates the order n of the resonance. The $n = 2$ cat's eye [blue curve in Fig. 8(c)] is similar to that of an unstrained vortex. The $n = 4$ cat's eye (orange curve) is also resolved. The width of the $n = 2$ and $n = 4$ resonant layers are different in action space due to different wave amplitudes excited by the initial perturbation. The relative size of these resonances would be an interesting topic for further study. Although higher-order resonances might be present in the experiments, they do not appear to influence the typical evolution of the quasi-flat vortex. In particular, the damping rate and trapping oscillations correspond closely to those observed in the strain-free case.

VI. SUMMARY AND CONCLUDING REMARKS

The inviscid damping of quadrupole perturbations on a quasi-flat vortex due to wave-vortex interactions with and without an externally imposed strain flow was investigated in the experiment and using numerical simulations. The experiments are done using strongly magnetized plasmas in a Penning–Malmberg trap, which exhibits the behavior of a 2D ideal fluid. The trap was designed specifically to be able to impose 2D external $\mathbf{E} \times \mathbf{B}$ flows on the plasma. The vortex core density and the extent of the surrounding halo vorticity were adjusted by varying the plasma compression using the rotating wall technique and the electron fill time, respectively.

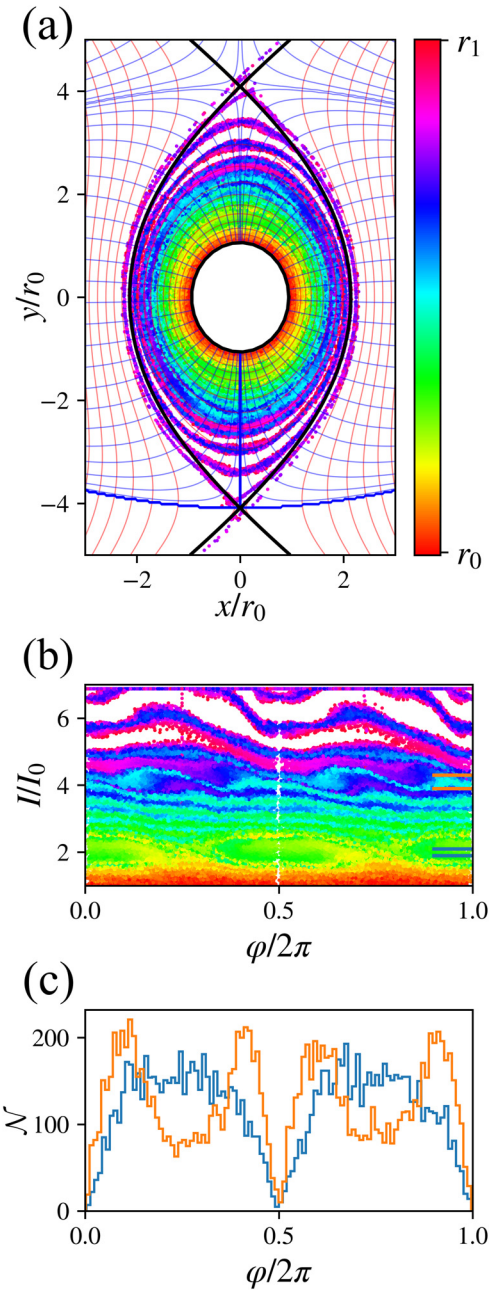

FIG. 8. (a) Numerical simulations of the halo of a strained vortex with the vorticity elements colored by their initial radial positions. for $\varepsilon = 0.03$ and $t = 168$. The halo extends to reach the separatrix. (b) The particle locations in (a) are converted to action-angle variables, (I, φ)-coordinates; and (c) the integrated number of particles in (b) are shown in two regions: $I/I_0 \in [1.9, 2.1]$ (blue) and $I/I_0 \in [3.9, 4.3]$ (orange). In (c), the number of peaks corresponds to n (i.e., blue, $n = 2$; and orange, $n = 4$).

The inviscid damping of quadrupole perturbations on an unstrained vortex was studied as a function of the halo vorticity profile. The damping rate was varied by controlling the radial profile of the halo vorticity. These data were compared with two theoretical descriptions, one assuming an idealized vortex patch with a small halo and the second an eigenfunction description of a smooth vortex with a monotonically decreasing halo as a function of radius. These two descriptions show good agreement with the observed damping rates for small halo amplitudes. The predictions diverge from the observations when the halo is large and a Lorentzian function is no longer a good approximation for the excitability spectrum. The eigenfunction description is more general; and thus, unsurprisingly, it agrees better with the observations than the simpler vortex-patch model.

A constant strain was then applied to a quasi-flat vortex with a small halo close to the vortex, and the dynamics of the vortex was studied close to the strained elliptical equilibrium. The initial amplitude of the quadrupole perturbation was created by linearly ramping the strain to a hold value. It was found that, when the holding strain value was varied, the damping rate remained unchanged, while the wave frequency was modified due to the shift of equilibrium. In the phase space of action-angle coordinates, the lowest order resonance exhibits the same dynamics with and without applied strain. The damping rate is strongly dependent upon the slope of the halo as a function of radius. When the strain is applied, the equilibrium for the vortex changes. However, the vorticity distribution as a function of the vortex element's action is conserved due to adiabaticity. Therefore, the damping rate is also preserved even with the applied strain.

In this work, both the elliptical perturbation and the applied strain [Eq. (3)] had the same mode number ($m = 2$). If the applied strain and perturbation were to have different mode numbers, the effect on the damping rate could be stronger.

Two additional damping mechanisms were explored, namely, the evaporation of vorticity across the separatrix and higher-order resonances due to vorticity at large values of the action. Trapping oscillations are observed in the experiments, which cause evaporation, and higher-order resonances are observed in numerical simulations. Both mechanisms do not change the evolution of a quasi-flat vortex in the linear decay phase. In addition, evaporation eliminates the trapping oscillations at larger values of the strain. Future work needs to be done to clarify their roles for smoother vortices. Furthermore, the azimuthal variation here can be compared to the axial variation in the original 1D electrostatic Landau problem. With a proper modified electric field, a phenomenon like damping rate invariance and higher-order resonances should also be present. In the 1D electrostatic Landau problem, higher-order resonances matter more because they go lower into the velocity distribution allowing for more interaction. In contrast, our problem involves the higher-order resonances going out to larger radii where there are fewer particles.

These results indicate that the inviscid vortex damping mechanism described in Refs. 15, 16, and 18 applies more generally to vortices that are not isolated but rather influenced by external flows. This situation is known to occur in a broad range of physical systems including sheared $\mathbf{E} \times \mathbf{B}$ eddies in the edges of tokamak plasmas, vortices subject to Keplerian shear in astrophysical disks, perturbed geophysical polar vortices, and the more general case of eddies in turbulent flows. Due to the ubiquitous observation of such damping in the 8ST,[32,34] this collisionless damping mechanism is expected to be important in a wide variety of rotational flows in fluids and plasmas.

ACKNOWLEDGMENTS

This work is supported by the U.S. Department of Energy, Grant Nos. DE-SC0016532, DE-SC0018236, and NSF Grant No. PHY 2106332.

AUTHOR DECLARATIONS

Conflict of Interest

The authors have no conflicts to disclose.

DATA AVAILABILITY

The data that support the findings of this study are available from the corresponding author upon reasonable request.

REFERENCES

[1]L. Polvani, J. Wisdom, E. DeJong, and A. Ingersoll, Science **249**, 1393 (1990).
[2]D. G. Dritschel and B. Legras, Phys. Today **46**(3), 44 (1993).
[3]A. Simon, M. Wong, and A. Hsu, Geophys. Res. Lett. **46**, 3108, https://doi.org/10.1029/2019GL081961 (2019).
[4]M. Mester and J. Esler, J. Atmos. Sci. **77**, 1167 (2020).
[5]P. Godon and M. Livio, Astrophys. J. **523**, 350 (1999).
[6]R. Lovelace, H. Li, S. Colgate, and A. Nelson, Astrophys. J. **513**, 805 (1999).
[7]P. J. Armitage and W. Kley, *From Protoplanetary Disks to Planet Formation* (Springer, 2019).
[8]P. Terry, Rev. Mod. Phys. **72**, 109 (2000).
[9]P. Manz, M. Ramisch, and U. Stroth, Phys. Rev. Lett. **103**, 165004 (2009).
[10]S. Kida, J. Phys. Soc. Jpn. **50**, 3517 (1981).
[11]R. Trieling, M. Beckers, and G. Van Heijst, J. Fluid Mech. **345**, 165 (1997).
[12]B. Legras and D. G. Dritschel, Phys. Fluids A **3**, 845 (1991).
[13]D. G. Dritschel and B. Legras, Phys. Fluids A **3**, 855 (1991).
[14]D. W. Moore and P. G. Saffman, Proc. R. Soc. London, Ser. A **346**, 413 (1975).
[15]R. Briggs, J. Daugherty, and R. Levy, Phys. Fluids **13**, 421 (1970).
[16]D. Schecter, D. Dubin, A. Cass, C. Driscoll, I. Lansky, and T. O'Neil, Phys. Fluids **12**, 2397 (2000).
[17]S. L. Dizes, J. Fluid Mech. **406**, 175 (2000).
[18]N. Balmforth, S. G. L. Smith, and W. Young, J. Fluid Mech. **426**, 95 (2001).
[19]C. Driscoll and K. Fine, Phys. Fluids B **2**, 1359 (1990).
[20]F. F. Chen, *Introduction to Plasma Physics* (Springer Science & Business Media, 2012).
[21]W. M. Orr, Proc. R. Ir. Acad., Sect. A **27**, 69–138 (1907). https://www.jstor.org/stable/20490591.
[22]S. Brown and K. Stewartson, J. Fluid Mech. **100**, 811 (1980).
[23]A. P. Bassom and A. D. Gilbert, J. Fluid Mech. **371**, 109 (1998).
[24]N. S. Pillai and R. W. Gould, Phys. Rev. Lett. **73**, 2849 (1994).
[25]J. F. Lingevitch and A. J. Bernoff, Phys. Fluids **7**, 1015 (1995).
[26]A. Ashourvan and D. H. Dubin, Phys. Plasmas **21**, 052109 (2014).
[27]F. Anderegg, M. Affolter, A. Kabantsev, D. Dubin, A. Ashourvan, and C. Driscoll, Phys. Plasmas **23**, 055706 (2016).
[28]P. J. Morrison, Rev. Mod. Phys. **70**, 467 (1998).
[29]R. Chu, J. Wurtele, J. Notte, A. Peurrung, and J. Fajans, Phys. Fluids B **5**, 2378 (1993).
[30]N. Hurst, J. Danielson, D. Dubin, and C. Surko, Phys. Rev. Lett. **117**, 235001 (2016).
[31]N. Hurst, J. Danielson, and C. Surko, AIP Conf. Proc. **1928**, 020007 (2018).
[32]N. Hurst, J. Danielson, D. Dubin, and C. Surko, J. Fluid Mech. **848**, 256 (2018).

[33]N. Hurst, J. Danielson, D. Dubin, and C. Surko, Phys. Plasmas **27**, 042101 (2020).
[34]N. Hurst, J. Danielson, D. Dubin, and C. Surko, Phys. Rev. Fluids **6**, 054703 (2021).
[35]D. A. Schecter, *On the Dynamics of Inviscid Relaxation in 2D Fluids and Nonneutral Plasmas* (University of California, San Diego, 1999).
[36]B. V. Chirikov, Phys. Rep. **52**, 263 (1979).
[37]A. Rechester and M. Rosenbluth, Phys. Rev. Lett. **40**, 38 (1978).
[38]J. Wisdom, Astron. J. **85**, 1122 (1980).
[39]J. Danielson, T. Weber, and C. Surko, Phys. Plasmas **13**, 123502 (2006).
[40]A. Leonard, J. Comput. Phys. **37**, 289 (1980).